

# JGR Space Physics

## RESEARCH ARTICLE

10.1029/2021JA029540

### Key Points:

- Thermospheric mass densities from 2014 to 2020 are estimated from CASCade SmallSat and IONospheric Polar Explorer Global Navigation Satellite System (GNSS) precise orbits
- The high-resolution thermospheric mass densities inferred from commercial-off-the-shelf GNSS receivers are validated
- The density disturbances due to magnetospheric forcing are investigated for correlations and time-delay responses to models and indices

### Correspondence to:

S. Jin,  
[sgjin@nuist.edu.cn](mailto:sgjin@nuist.edu.cn);  
[sg.jin@yahoo.com](mailto:sg.jin@yahoo.com)

### Citation:

Calabia, A., & Jin, S. (2021). Thermospheric mass density disturbances due to magnetospheric forcing from 2014–2020 CASSIOPE precise orbits. *Journal of Geophysical Research: Space Physics*, 126, e2021JA029540. <https://doi.org/10.1029/2021JA029540>

Received 6 MAY 2021

Accepted 21 JUL 2021

### Author Contributions:

**Conceptualization:** Andrés Calabia, Shuanggen Jin  
**Data curation:** Andrés Calabia  
**Formal analysis:** Andrés Calabia  
**Funding acquisition:** Shuanggen Jin  
**Investigation:** Andrés Calabia  
**Methodology:** Andrés Calabia  
**Project Administration:** Shuanggen Jin  
**Software:** Andrés Calabia  
**Supervision:** Shuanggen Jin  
**Validation:** Shuanggen Jin  
**Visualization:** Andrés Calabia  
**Writing – original draft:** Andrés Calabia  
**Writing – review & editing:** Shuanggen Jin

## Thermospheric Mass Density Disturbances Due to Magnetospheric Forcing From 2014–2020 CASSIOPE Precise Orbits

Andrés Calabia<sup>1</sup>  and Shuanggen Jin<sup>1,2</sup> 

<sup>1</sup>School of Remote Sensing and Geomatics Engineering, Nanjing University of Information Science and Technology, Nanjing, China, <sup>2</sup>Shanghai Astronomical Observatory, Chinese Academy of Sciences, Shanghai, China

**Abstract** Long-term thermospheric mass density disturbances due to magnetospheric forcing are not clear due to a lack of measurement data and imprecise models. In this study, the Global Navigation Satellite System (GNSS) precise orbits of CASCade SmallSat and IONospheric Polar Explorer (CASSIOPE) are used to infer high-resolution thermospheric mass densities between the years 2014 and 2020. The CASSIOPE densities are comprehensively validated at altitudes from 325 to 425 km at intervals of 25 km with the High Accuracy Satellite Drag Model (HASDM) density database, and further compared with the Naval Research Laboratory Mass Spectrometer and Incoherent Scatter Radar Exosphere/2000 (NRLMSISE-00) and the Jacchia-Bowman/2008 (JB2008) empirical models. The CASSIOPE densities are very similar to the HASDM and JB2008 densities, while the NRLMSISE-00 largely overestimates (~150%) during low solar-flux conditions. For density values above  $\sim 10^{-12}$  kg/m<sup>3</sup>, the correlation of CASSIOPE with HASDM is ~5% better than the models, and the standard deviation is within 10% of the background density. For density values below  $\sim 10^{-12}$  kg/m<sup>3</sup>, systematic errors have shown to reduce the precision of the CASSIOPE densities. By setting geomagnetic contributions to zero in the models, the density disturbances due to magnetospheric forcing are isolated from the CASSIOPE time-series, allowing investigation into the correlations and time-delay responses to the models and to the merging electric field ( $E_m$ ). A new linear dependence of the time delay to the  $E_m$  was found and then parameterized in this study. Time delays occurred at the 4–7 h range during geomagnetic storms, and at 9–11 h during quiet conditions; neither had significant dependence on altitude. The results represent the validation of the first high-resolution thermospheric mass density estimates inferred from commercial-off-the-shelf GNSS receivers.

## 1. Introduction

The characterization of the Earth's thermosphere, especially during geomagnetic storms, is essential for applications such as Low Earth Orbit (LEO) satellite tracking and space weather research; thermosphere models are routinely used as input in precise orbit determination (POD) schemes so that the position and velocity of orbiting satellites can be accurately estimated (Montenbruck & Gill, 2013). However, positioning errors caused by uncertainties in the existing models are still a major concern (Anderson et al., 2009; Jin et al., 2017; Calabia et al., 2020), largely due to the limited quality and quantity of data. Previously, thermospheric mass density variations have been monitored by a variety of instruments and methods (Jin et al., 2018), but only accelerometers on-board satellites have provided enough resolution to study high-cadence disturbances caused by, for example, geomagnetic storms. The first high-resolution studies based on accelerometers were by Marcos and Forbes (1985), and numerous scientific outcomes have followed since then (e.g., Bruinsma & Biancale, 2003; Calabia & Jin, 2016a; Doornbos et al., 2010; Mehta et al., 2017), in particular about disturbances caused by geomagnetic storms (e.g., Bruinsma et al., 2006; Calabia & Jin, 2019; Lühr et al., 2004; Sutton et al., 2005).

The upper-atmosphere is mainly composed of two parts, the thermosphere and the ionosphere. In the thermosphere, photoabsorption, photoionization, and photodissociation of molecules through extreme ultraviolet radiation (EUV) create the ions of the ionosphere, and thermal energy-transfer from ions to neutral particles drives the regular dynamics. However, this complex system is highly variable in space and time, and the physical processes and corresponding mechanisms are not well understood (Heelis & Maute, 2020;



**Figure 1.** Orbital altitudes (left axis) of the satellites capable to estimate high-resolution thermospheric mass densities. The CAScade SmallSat and IOnospheric Polar Explorer (CASSIOPE) satellite covers altitudes from ~330 to ~1,300 km due to its elliptical orbit, while the others have circular orbits. The 81-days mean solar flux F10.7 index is show in red (right axis).

Palmroth et al., 2021). These processes, generally called space weather, can influence on several segments of the economy negatively; satellites, communications, electric power distribution, airline industry, and Global Navigation Satellite Systems (GNSS) users. This shows how important it is for us to study the possible detrimental impacts scientifically, then to implement and maintain reliable and integrated geodetic space weather monitoring (Jin et al., 2011; Okoh et al., 2018; Blossfeld et al., 2019).

While the regular dynamics of the thermosphere are mainly driven by the day-night and annual cycles of solar EUV (Calabia & Jin, 2016a; Qian & Solomon, 2012), the effects of geomagnetic storms can cause an increase in its density of up to 800% (Bruinsma et al., 2006; Calabia & Jin, 2016b; Liu & Lühr, 2005; Sutton et al., 2005). Usually, geomagnetic storms begin as a high latitude event located at the aurora region. Shortly after the beginning of the storm, the whole Earth's thermosphere responds with southward-traveling gravity waves, and a global density increase occurs. This can last anywhere between several hours to multiple days. Many studies have shown thermospheric variations during geomagnetic storms are difficult to investigate due to a lack of measurement data and large uncertainties in the models (e.g., Calabia et al., 2020; Chen et al., 2014; Jackson et al., 2020; Oliveira & Zesta, 2019).

On-board satellite accelerometers can measure non-gravitational accelerations and derive thermospheric mass density variation data with unprecedented details. However, the high instrumental costs and other technical issues (Bruinsma et al., 2004; Calabia & Jin, 2017; Calabia et al., 2015; Siemes et al., 2016) have limited these technology payloads to be carried by only a small number of satellites. In the last 20 years, the only missions carrying accelerometers were Challenging Minisatellite Payload (CHAMP), Gravity Recovery and Climate Experiment (GRACE), Gravity field and steady-state ocean circulation explorer (GOCE), and Swarm (Figure 1). Currently, continuous high accuracy GNSS observation on-board LEO satellites has proven the capability to measure high-cadence, non-gravitational accelerations, and then estimate densities at a high resolution (Calabia & Jin, 2017, 2021a; Calabia et al., 2015; Li & Lei, 2020; van den IJssel et al., 2020; Yuan et al., 2019).

With the increasing number of LEO satellites being equipped with a high-precision GNSS receivers, and therefore more enhanced data processing and orbit determination strategies, GNSS-based thermospheric mass densities may become an essential data to effectively monitor global thermospheric fluctuations; GNSS Thermosphere Insitu Sensing (GNSS-TIS). Recently, for instance, commercial-off-the-shelf, geodetic grade, dual-frequency GNSS receivers on board small satellites have demonstrated their full capability for geodetic observations. These come at an affordable cost for low-budget space missions (Jin & Su, 2020; Kim & Langley, 2019), and can be used to retrieve high-resolution thermospheric mass densities (Calabia & Jin, 2021a). It is very likely that in the near future, these upgraded GNSS receivers will become a common

payload in most satellite missions, and their high-precision, high-accuracy GNSS ephemeris products will be used as standard to estimate thermospheric mass densities.

In Calabia and Jin (2021a), the GNSS ephemeris of the CAScade SmallSat and IOnospheric Polar Explorer (CASSIOPE) satellite were used to investigate at high resolution the thermosphere's response to the geomagnetic storm of February 2014. The CASSIOPE satellite was launched on September 29, 2013. It is the first mission to cover both telecommunications and scientific research purposes (Yau et al., 2006). The main scientific objectives of the CASSIOPE mission are to better understand the complex processes that occur in the upper atmosphere, while performing high-speed communications at the same time. It is important to note that the initial purpose of the GNSS instruments on-board the CASSIOPE satellite were not intended to retrieve thermospheric mass densities; the GNSS-based densities could become an exceptional secondary data to assist in analysis and validation of the other payload measurement data.

In this study, a new thermospheric mass density data set is estimated from CASSIOPE GNSS precise orbits during the period 2014 to 2020 and validated by the High Accuracy Satellite Drag Model (HASDM) density data set (Tobiska et al., 2021). The ratio (quotient) between the CASSIOPE and the HASDM densities is compared with that of the Naval Research Laboratory Mass Spectrometer and Incoherent Scatter Radar Exosphere/2000 (NRLMSISE-00) (Picone et al., 2002) and the Jacchia-Bowman/2008 (JB2008) (Bowman et al., 2008) empirical models, that is, NRLMSISE-00/HASDM and JB2008/HASDM, respectively. The trends and standard deviations of the ratios from 325 to 425 km altitude at increments of 25 km are analyzed. Then, by setting geomagnetic contributions to zero in the models, the “quiet” background is removed from the time-series to investigate the long-term correlations and time-lags of the disturbances due to magnetospheric forcing. In the following sections, the data and techniques used for thermospheric mass density retrieval are described. Then, the results as a function of time and altitude are analyzed, and the statistical comparisons for the validation and the assessment are performed. Finally, issues raised by the analyses, and some suggestions for future progression is discussed.

## 2. Data and Methods

### 2.1. Density Estimation From CASSIOPE GNSS Precise Orbits

GNSS data from the CASSIOPE spacecraft are used to obtain the density estimates during the period 2014–2020. The CASSIOPE satellite is equipped with 5 commercial-off-the-shelf dual-frequency GNSS receivers (L1 C/A and L2 P) tracking up to 12 Global Position System (GPS) satellites. The GNSS instrument is called GPS Attitude, Position, and profiling experiment (GAP), and is used for spacecraft position as well as for attitude determination and for ionospheric radio occultation. Positioning errors are within the range of a few decimeters and a few millimeters for individual pseudorange and carrier phase measurements, respectively. In this study, the precise orbit solutions computed from Montenbruck et al. (2019) are used. The authors computed the precise positions and velocities at a second interval in a reduced-dynamic approach with float-ambiguity estimation. The CASSIOPE mission has a slightly eccentric polar orbit of 81° inclination, with altitudes ranging from approximately 1,400 km in the apogee to 325 km in the perigee. Due to its precessing orbit, the in-situ measurements cover all longitudes and local solar time (LST) locations. Figure 1 shows the orbital altitudes of the CASSIOPE satellite during the declining phase of the solar cycle 24.

Based on the method of Calabia et al. (2015), GNSS-based total accelerations are retrieved through numerical interpolation of the precise velocity products. Subsequently, air-drag forces are obtained by removing gravitational and radiation-pressure force-models, which can be finally used for density estimation. More details of the methodology can be found in Appendix A and Appendix B. The most important sources of error in this method are caused by the accuracy of the velocity products, and the errors caused by the drag coefficient and the thermospheric winds models. The errors in the precise velocities are usually originated in the POD scheme (stochastic least squares adjustment between models and GNSS observables) and can cause noise and outliers in the resulting non-gravitational accelerations (Calabia et al., 2015). Here, in order to mitigate high-cadence variations, noises, and possible outliers, a 6 min mean-average running filter is applied. We tested different filtering lengths for different periods along the time-series, and the optimal length was a 6 min averaging window, as we can see in Figure 2. Other lengths provide too average results or too large residual noises. In this way, the comparisons with the empirical models will be more suitable,

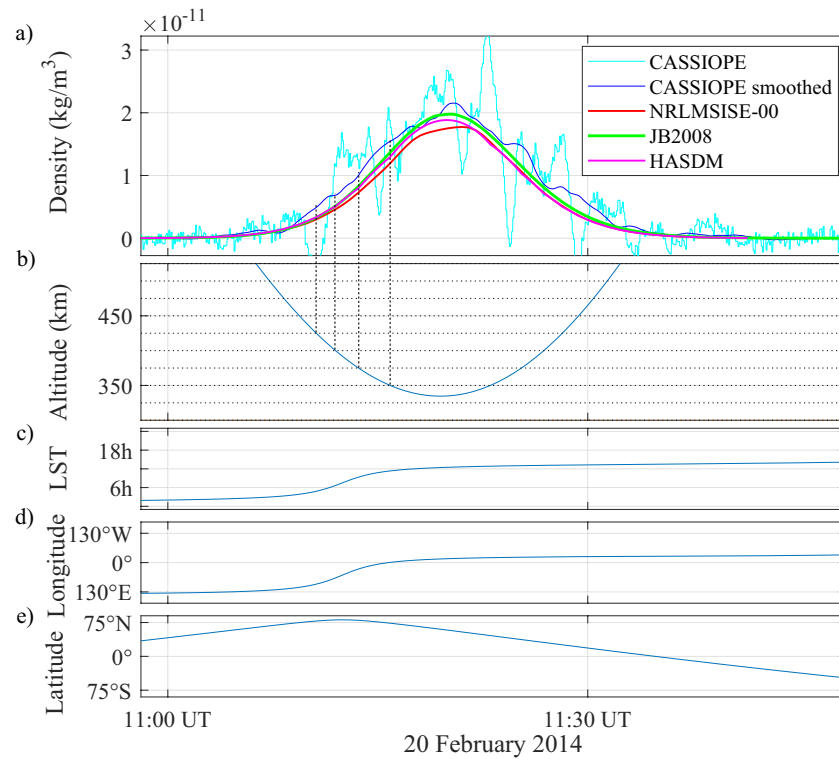


**Figure 2.** Thermospheric information with (a) density estimates from CAScade SmallSat and IOnospheric Polar Explorer (CASSIOPE) and models, (b) altitudes, (c) local solar time (LST), (d) longitude, and (e) latitude along the CASSIOPE orbit on February 20, 2014. In (a), at the inbound orbit, a set of four samples can be identified at steps of 25 km in altitude. For the illustrated window,  $Dst = -90$  nT, and  $F_{10.7} = 153$  sfu.

since these can only provide an averaged state of the actual variations. The errors due to zonal and meridional winds are estimated at 1% and 4% per 100 m/s wind error, respectively (Bruinsma et al., 2004, 2006), while drag coefficients under different gas-surface interaction assumptions are expected to differ by  $\sim 15\%$ , during solar minimum conditions, and by  $\sim 2\%$ – $3\%$ , during solar maximum (March et al., 2019a; Mehta et al., 2014, 2017). Other minor systematic errors in the densities are directly connected to the aerodynamic modeling of the satellite (March et al., 2019b). In this study, a variable drag coefficient in terms of solar flux and altitude (Pardini et al., 2006) is used for satellites with hexagonal-prism shapes (Walker et al., 2014), and the density estimates are re-scaled to match with that of the HASDM data set, which is considered the most accurate up-to-date. According to this, under quiet magnetospheric conditions, a higher accuracy compared to using a constant drag coefficient and a flat plate model is expected; within 10% of the background density (Bruinsma et al., 2006).

## 2.2. Analysis Methods and Models

To validate and assess the CASSIOPE densities, the recently released HASDM data set (Tobiska et al., 2021) is used as the control, and its quotient of densities (CASSIOPE/HASDM) is compared with that given by the NRLMSISE-00 and the JB2008 models, that is, NRLMSISE-00/HASDM and JB2008/HASDM, respectively. First to be analyzed is the distribution of the data in terms of LST and geographical coordinates with a spatial histogram analysis. Then, a Pearson's linear correlation analysis is performed between the HASDM densities and the densities from the CASSIOPE and the models. The paper also further compares the fluctuations and deviations of the ratio along the time-series of the data, applying both a 30-days mean-average and a 30-days standard-deviation running filters. The general form for the mean-average running-window filter is:

$$Filt(x_i) = \sum_{j=i-a}^{i+a} \frac{x_j}{(2a+1)} \quad (1)$$

In this equation,  $x_i$  is the time-series to filter at each sampling index  $i$ ,  $a$  is half of the increment of time for each corresponding running-window. The standard deviation is calculated with similar form of Equation 1. The resulting statistics provide means to assess the accuracy of the new CASSIOPE density estimates. Finally, the analysis to assess and investigate the disturbances due to magnetospheric forcing is introduced in the next section. The used models are presented as follows:

1. The HASDM values are derived from several dozens of calibration satellites, which are validated weekly by the U.S. Air Force Space Command and Space Environment Technologies (SET). This validation is able to recreate the densities of the global atmosphere, and the resulting data are provided every 3 h at a grid size of  $10^\circ \times 15^\circ$  (latitude, longitude), with 25 km altitude steps between 175 and 825 km. This data set is called the SET-HASDM density database. Due to the high accuracy of the HASDM data set (Tobiska et al., 2021), the differences to these, along with the comparisons to the existing models, will allow a reasonable validation and uncertainty assessment of the new CASSIOPE densities.
2. The NRLMSISE-00 model is the standard model of the Earth's atmosphere to aid predictions of satellite orbital decay due to atmospheric drag, and it has widely been used in numerous research studies and applications (e.g., Emmert & Picone, 2010; Horvath & Lovell, 2018; Pardini et al., 2006; Pilinski et al., 2011). This model is based on averaged data from several measurement techniques, including mass spectrometers, incoherent scatter radars, satellite drag data, and solar ultraviolet occultation. More details about the background database of the NRLMSISE-00 model can be found in Picone et al. (2002).
3. While NRLMSISE-00 uses the exponential Bates vertical profile (Bates, 1959), the Jacchia-Bowman/2008 (JB2008) model represents the asymptotic behavior of the upper thermosphere with the arctangent function (Bowman et al., 2008). The measurement data sources employed in the JB2008 model include the Air Force daily density values (Bowman et al., 2004), the HASDM values (Bowman & Storz, 2003; Storz et al., 2005), and the CHAMP and GRACE accelerometer-based densities. Recent studies have shown the very good performance of JB2008 against NRLMSISE-00 (e.g., Calabia & Jin, 2019).

### 2.3. Density Disturbances Due to Magnetospheric Forcing

The disturbance storm time (Dst) index, in units of nT, is commonly used in upper atmosphere modeling during geomagnetic storms. Usually, Dst decreases as ring current energy increases, following a southward-turning of the interplanetary magnetic field (IMF). However, the Dst index lacks time delay for early warnings of hazardous variability of the thermospheric mass density. Another suitable parameter that closely correlates with mass density variations during geomagnetic storms, and that has a larger time delay, is the merging electric field  $E_m$  (Calabia & Jin, 2019, 2021a; Liu et al., 2010), in units of mV/m. The  $E_m$  index assumes that there is an equal magnitude of the electric field in the solar wind, the magnetosheath, and on the magnetospheric sides of the magnetopause (Kan & Lee, 1979). The  $E_m$  index is a physical quantity that can be easily obtained from solar wind and IMF data, and it correlates significantly with density changes during all storm phases.

To compare high-cadence density disturbances due to magnetospheric forcing with the fluctuations of the  $E_m$  index and models, we first remove the “quiet” background from the time-series. The “quiet” background refers to that of negligible geomagnetic conditions. The “quiet” background is estimated by computing the models at the same locations and times, but with the geomagnetic inputs set to zero. Then, a 30-days mean-average running filter is applied to both densities and  $E_m$  time-series to remove the long-term variations. It is expected that the resulting short-term variations of both densities and  $E_m$  time-series will contain the typical 27, 14, and 9-day periods caused by the magnetospheric forcing (Calabia & Jin, 2020). Long-term variations of solar wind parameters and geomagnetic activity are usually delayed by two years in time with the activity of the solar-flux cycle (Echer et al., 2004), and its contribution to thermospheric density variability is difficult to detect due to large residuals in the models. Then, a correlation-delay study of the resulting short-term variations (<30 days) at different altitudes is performed, to reveal the best possible fit at different lag times within a range of  $\pm 18$  h. In this step, the sequential calculation of the Pearson's linear correlation coefficient using a 30-days running window to obtain the time delays between the filtered densities and the  $E_m$  index at maximum correlation is used. Finally, the fitting parameters are calculated for the magnitude  $\rho_{E_m}^*$  ( $\text{kg}/\text{m}^3$ ) and time delay  $\delta_{E_m}$  (h) of the density disturbances due to magnetospheric forcing

**Table 1**  
Scale Factor Applied to  $C_D$  w.r.t. That of Estimated by Calabia and Jin (2021a)

Altitude (km)	$C_D$ scale factor w.r.t. Calabia and Jin (2020)
325	0.86
350	0.82
375	0.81
400	0.78
425	0.77

in terms of the  $E_m$  index (mV/m) and the solar flux  $F_{10.7}$  index (s.f.u.) (sfu =  $10^{-22}$  Wm<sup>-2</sup>/Hz) as follows:

$$\rho_{E_m}^* (F_{10.7}, E_m) = \frac{F_{10.7}(t)}{100} \cdot [p1 \cdot E_m (t + \delta_{E_m}) + p2] \cdot 10^{-15} \quad (2a)$$

$$\delta_{E_m} (\rho_{E_m}^*) = d1 \cdot \rho_{E_m}^* \cdot 10^{13} + d2 \quad (2b)$$

In these equations, p1, p2, d1, and d2 are the parameters, and  $t$  is the Co-ordinated Universal Time (UTC) in hours.

### 3. Results and Analysis

The thermospheric mass densities from CASSIOPE GNSS precise orbits are estimated at a second interval for the period 2014–2020. Figure 2a shows the resulting density estimates from CASSIOPE GNSS along with the HASDM database and the models for a case example on February 20, 2014. The altitudes of the satellite along the orbit are shown in Figure 2b. During this period, CASSIOPE's orbital descending node ( $\mathcal{C}$ ) was approximately located at 13 h LST (Figure 2c), and the latitudes and longitudes of the satellite along the orbit are shown in Figures 2d and 2e. In this figure, clear differences between estimates and models can be seen around the perigee location (i.e., location of highest density values along orbit). These differences are mostly caused by inaccuracies in the models during geomagnetic storms. A deeper analysis for this particular storm can be found in Calabia and Jin (2021a).

In this study, the analysis of differences with the HASDM database have shown that scaling the CASSIOPE's drag coefficient of Calabia and Jin (2021a) by approximately 0.8 would provide a better match. Using this, the estimated altitude dependence on this scaling factor is given in Table 1. The scale factors at each altitude were estimated as the median value of the rate between the time-series. In Figure 3, the count of revisiting days is presented as spatial histograms in terms of altitude, latitude, longitude, and LST, for both low and high solar-flux conditions during the period 2014–2020. Here, both inbound and outbound orbits are included. The count has been binned at four altitude ranges ( $h_1 < 350 < h_2 < 400 < h_3 < 450 < h_4 < 500$  km), and most of the bins have at least 30 days or more. The resulting count is suitable for modeling schemes, statistical analyses, and data validation.

The correlation coefficients for the CASSIOPE, JB2008, and NRLMSISE-00 densities with respect to the HASDM densities, at different altitudes, are shown in Table 2. The best match is given by the CASSIOPE densities at the lowest altitude (325 km), with a correlation of 99.4%. At this altitude, the JB2008 and NRLMSISE-00 densities correlate 1.4% and 3.5% lower, respectively. Then, at 350 km altitude, the CASIOPE densities still provide better correlation, with 0.5% and 3% higher values than that given by the JB2008 and NRLMSISE-00 models, respectively. From 375 km and above, the correlation given by the JB2008 model reaches a similar value to that of the CASSIOPE densities, while the NRLMSISE-00 model reaches the similar correlation at 425 km.

#### 3.1. Ratio of Densities Relative to HASDM

Figures 4–8 show the CASSIOPE densities and those from the NRLMSISE-00 and JB2008 models, relative to the HASDM densities, for altitudes ranging from 325 to 425 km at steps of 25 km. Since the samples from the outbound orbits provide similar results, only the samples retrieved from the inbound orbits are shown. The three top panels picture the density ratios of CASSIOPE, NRLMSISE-00, and JB2008, and the solution of the 30-days mean-average running filter. Additions and subtractions of the 30-days standard-deviation running filter to the mean averages are also included, and their magnitudes in the logarithmic scale are shown in the fourth panels. The bottom panels show the background densities.

In Figure 4, data gaps are caused by the variable altitude of the satellite's perigee, which sometimes does not reach 325 km altitude. For density values above  $\sim 10^{-12}$  kg/m<sup>3</sup>, the CASSIOPE densities have smaller ratios and smaller standard deviations than that of NRLMSISE-00 and JB2008. For densities above  $\sim 10^{-11}$  kg/m<sup>3</sup>,

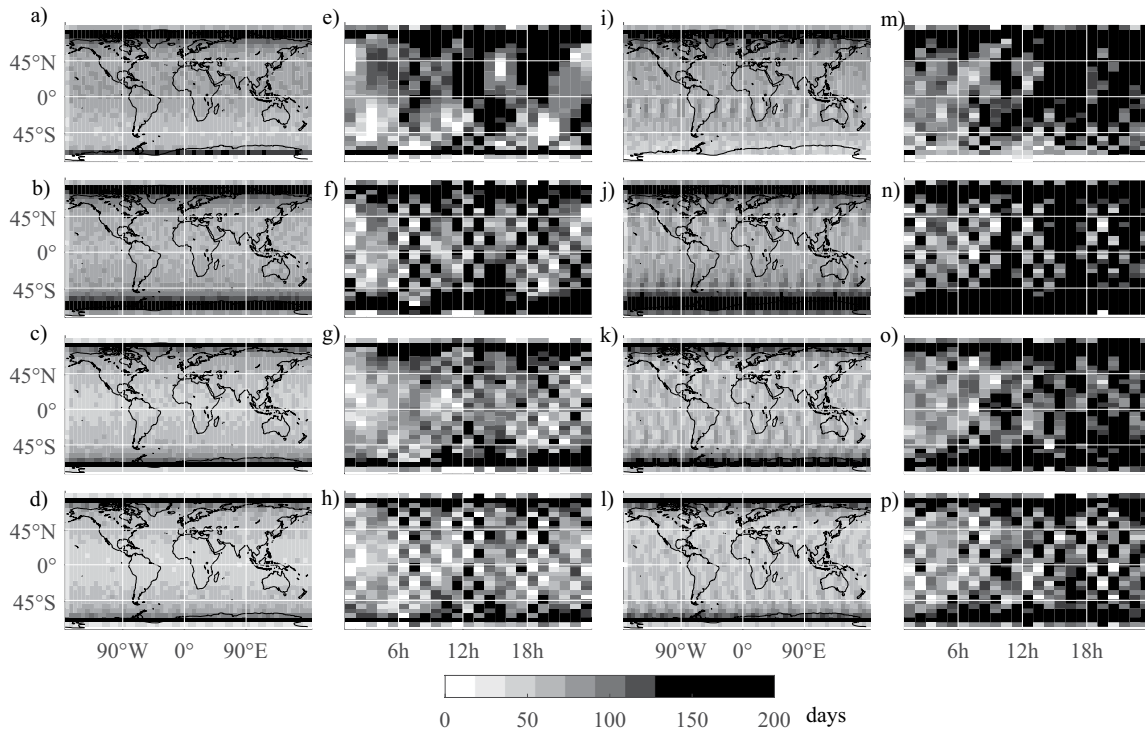


**Figure 3.** Spatial histograms of revisiting days as seen from CAScade SmallSat and IONospheric Polar Explorer (CASSIOPE)'s orbits for the period 2014–2020. From top to bottom, 4 altitude ranges by rows: (a, e, i, and m)  $h_1 < 350$  km, (b, f, j, and n)  $350 < h_2 < 400$  km, (c, g, k, and o)  $400 < h_3 < 450$  km, and (d, h, l, and p)  $450 < h_4 < 500$  km. Low solar flux conditions ( $F_{10.7} < 75$  s.f.u.) are on the left panels (a–h), and high solar flux conditions ( $F_{10.7} > 75$  s.f.u.) are on the right panels (i–p). First and third columns (a–d, and i–l) are the geographical coordinates ( $6^\circ \times 6^\circ$  bin), second and fourth columns (e–h, and m–p) are the local solar time (LST) distributions ( $6^\circ \times 1$ -h bin).

it is remarkable that the standard deviations of CASSIOPE can reach 2% of the background density. However, for density values below  $\sim 10^{-12}$  kg/m<sup>3</sup>, systematic errors seem to reduce the precision of the CASSIOPE densities. It can be seen that, during low solar flux conditions, the variation of the ratio fluctuates largely (e.g.,  $\pm 25\%$  in January 2018, 50% in January 2019), but the standard deviation has a moderate increase (below 10%).

In Figures 5c–8c, the fluctuation of CASSIOPE densities show a clear periodic trend of around 2 months, which increases in amplitude with a low-density background. A similar variation, but very less pronounced, is found in the models, with similar variations on May 2017, January 2019, etc. The exact period of 62.5 days

was estimated by fast Fourier transform (FFT) spectral density analysis. This period was identified with that of the latitudinal variation (periodograms not included). The increases of the density ratio are correlated with higher latitudes, while the ratios decrease with lower latitudes. The existence of systematic errors suggests potential to improve results further.

The similarities between the JB2008 and the HASDM densities are significant, in comparison to the NRLMSISE-00 model. This is expected, since the HASDM values are included as empirical basis of the JB2008 model. The discrepancies to the NRLMSISE-00 model show different trends of the ratio, and a variable amplitude of the standard deviation. In general, larger ratios and larger standard deviations at all altitudes are seen from the NRLMSISE-00 densities, in comparison to the JB2008 (full time-series) and the CASSIOPE (density values above  $\sim 10^{-12}$  kg/m<sup>3</sup>) densities. For the CASSIOPE and the JB2008 models, the ratio is centered to unit, while the NRLMSISE-00 appears to provide larger ratios during low solar

**Table 2**  
Correlation of CASSIOPE, NRLMSISE-00, and JB2008 Densities to the HASDM Densities for the Period 2014–2020

Altitude (km)	Cassiope	NRLMSISE-00	JB2008
325	0.994	0.959	0.980
350	0.992	0.962	0.987
375	0.987	0.961	0.986
400	0.977	0.961	0.985
425	0.956	0.960	0.985

CASSIOPE, CAScade SmallSat and IONospheric Polar Explorer; HASDM, High Accuracy Satellite Drag Model; JB2008, Jacchia-Bowman/2008; NRLMSISE-00, Naval Research Laboratory Mass Spectrometer and Incoherent Scatter Radar Exosphere/2000.

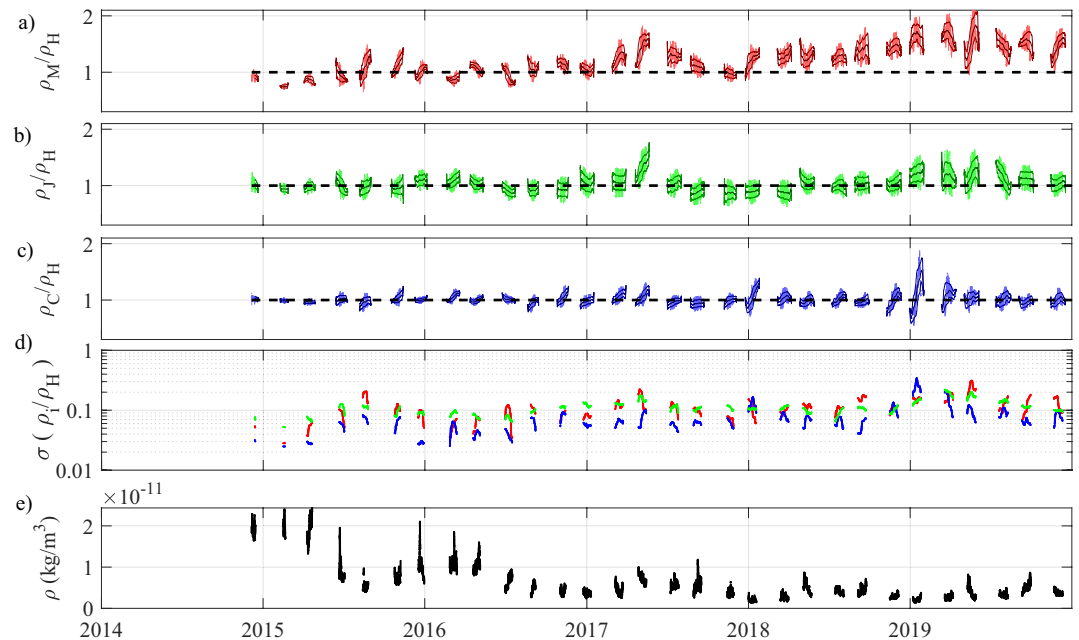


**Figure 4.** The (a) Naval Research Laboratory Mass Spectrometer and Incoherent Scatter Radar Exosphere/2000 (NRLMSISE-00), (b) Jacchia-Bowman/2008 (JB2008), and (c) CAScade SmallSat and IOnospheric Polar Explorer (CASSIOPE) densities relative to the High Accuracy Satellite Drag Model (HASDM) densities at 325 km altitude. Samples from inbound orbits. Values of (a–d) are dimensionless. Panels (a and b) include the 30-days running window median averages ( $\mu$ ) and standard deviations ( $\mu \pm \sigma$ ) of the ratios. Panel (d) shows the standard deviations ( $i = M, J, C$ ) for comparison, and the background density is shown in (e).

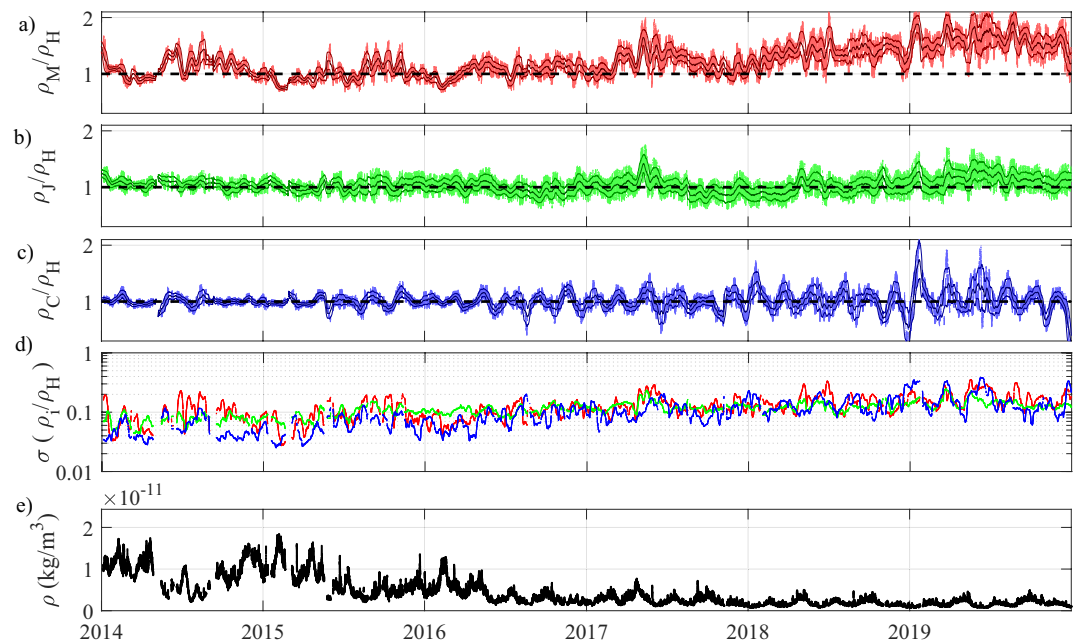


**Figure 5.** The (a) Naval Research Laboratory Mass Spectrometer and Incoherent Scatter Radar Exosphere/2000 (NRLMSISE-00), (b) Jacchia-Bowman/2008 (JB2008), and (c) CAScade SmallSat and IOnospheric Polar Explorer (CASSIOPE) densities relative to the High Accuracy Satellite Drag Model (HASDM) densities at 350 km altitude. Samples from inbound orbits. Values of (a–d) are dimensionless. Panels (a and b) include the 30-days running window median averages ( $\mu$ ) and standard deviations ( $\mu \pm \sigma$ ) of the ratios. Panel (d) shows the standard deviations ( $i = M, J, C$ ) for comparison, and the background density is shown in (e).

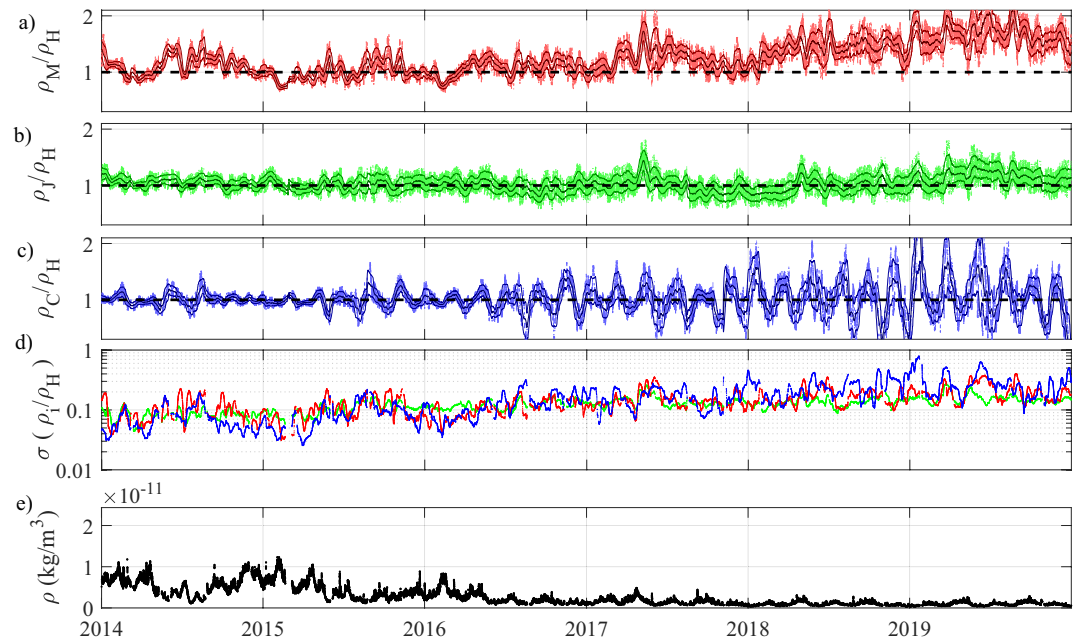


**Figure 6.** The (a) Naval Research Laboratory Mass Spectrometer and Incoherent Scatter Radar Exosphere/2000 (NRLMSISE-00), (b) Jacchia-Bowman/2008 (JB2008), and (c) CAScade SmallSat and IONospheric Polar Explorer (CASSIOPE) densities relative to the High Accuracy Satellite Drag Model (HASDM) densities at 375 km altitude. Samples from inbound orbits. Values of (a–d) are dimensionless. Panels (a and b) include the 30-days running window median averages ( $\mu$ ) and standard deviations ( $\mu \pm \sigma$ ) of the ratios. Panel (d) shows the standard deviations ( $i = M, J, C$ ) for comparison, and the background density is shown in (e).

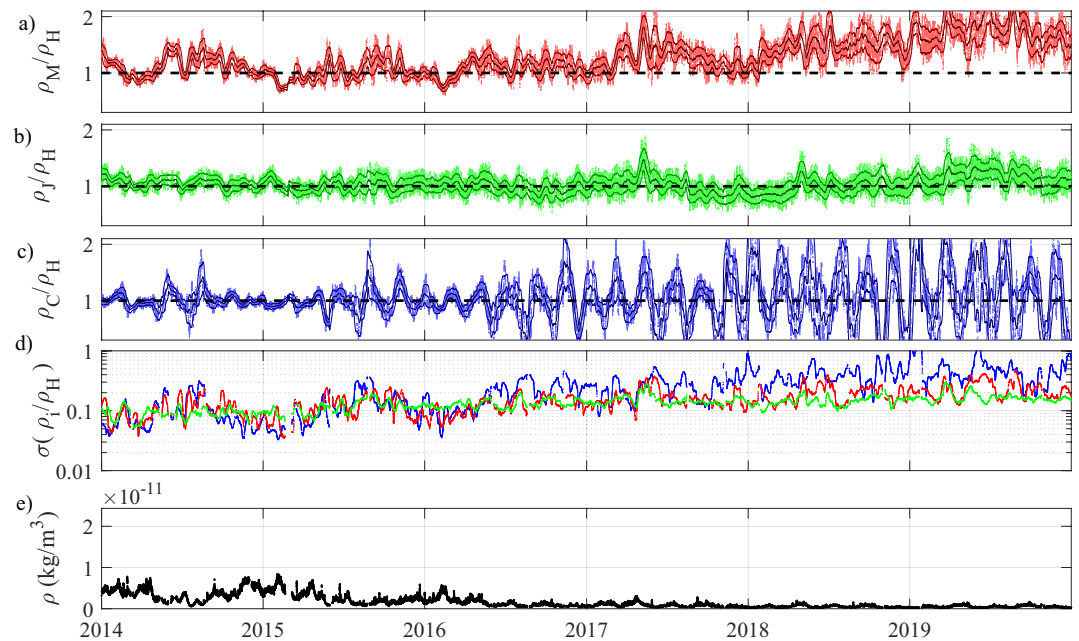


**Figure 7.** The (a) Naval Research Laboratory Mass Spectrometer and Incoherent Scatter Radar Exosphere/2000 (NRLMSISE-00), (b) Jacchia-Bowman/2008 (JB2008), and (c) CAScade SmallSat and IONospheric Polar Explorer (CASSIOPE) densities relative to the High Accuracy Satellite Drag Model (HASDM) densities at 400 km altitude. Samples from inbound orbits. Values of (a–d) are dimensionless. Panels (a and b) include the 30-days running window median averages ( $\mu$ ) and standard deviations ( $\mu \pm \sigma$ ) of the ratios. Panel (d) shows the standard deviations ( $i = M, J, C$ ) for comparison, and the background density is shown in (e).

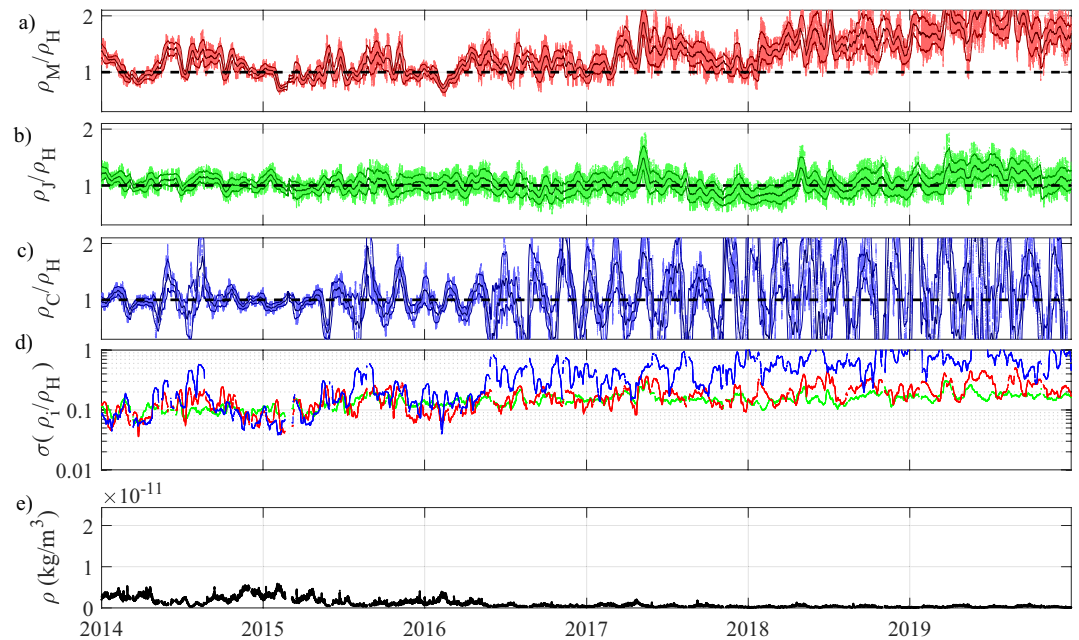


**Figure 8.** The (a) Naval Research Laboratory Mass Spectrometer and Incoherent Scatter Radar Exosphere/2000 (NRLMSISE-00), (b) Jacchia-Bowman/2008 (JB2008), and (c) CAScade SmallSat and IOnospheric Polar Explorer (CASSIOPE) densities relative to the High Accuracy Satellite Drag Model (HASDM) densities at 425 km altitude. Samples from inbound orbits. Values of (a–d) are dimensionless. Panels (a and b) include the 30-days running window median averages ( $\mu$ ) and standard deviations ( $\mu \pm \sigma$ ) of the ratios. Panel (d) shows the standard deviations ( $i = M, J, C$ ) for comparison, and the background density is shown in (e).

flux periods. The NRLMSISE-00 densities seem to overestimate the HASDM densities up to 150% during 2018–2019, while the JB2008 densities only 130%.

A visual summary of the statistics from Figures 4–8 is presented in Figure 9, with a Red-Green-Blue (RGB) image composite of the 30-days mean-averages of the ratios and corresponding standard deviations. The RGB composite is an optimal method to visualize distributions of data that overlap the same dimensional space. In this way, a non-overlapping data set shows its own color, that is, blue color for CASSIOPE, green for JB2008, and red for NRLMSISE-00. Then, the cyan color results from overlapping CASSIOPE (blue) with JB2008 (green), the yellow from overlapping JB2008 (green) with NRLMSISE-00 (red), and the magenta from overlapping NRLMSISE-00 (red) with CASSIOPE (blue). The white color indicates the overlapping scatters of all three datasets. Moreover, different saturations would provide different colors. On the left panels we show the ratios of the densities, and in the right panels the standard deviations. For the left panels, note the logarithmic scale in the background density (y-axis), for the standard deviations, both axes are in logarithmic scale. On the right panels, we also include the logarithmic fit of the standard deviations, so that the different distributions can be easy seen. From top to bottom, the 5 different altitudes show the resulting ranges of density, centered in larger densities ( $\sim 10^{-11}$  kg/m<sup>3</sup>) at the top panels, and moving to lower densities ( $\sim 10^{-13}$  kg/m<sup>3</sup>) at the bottom panels.

In regards to the density ratios (Figure 9, left panels), the NRLMSISE-00 densities (red) overestimate the HASDM densities by approximately 150% for density values below  $10^{-12}$  kg/m<sup>3</sup>. It is important to note this overestimation shows a possible dependence on altitude. The second clear feature is the large and centered spread of the CASSIOPE ratio for density values below  $10^{-12}$  kg/m<sup>3</sup>. This is caused by the systematic variation of 62.5 days' period, which is seen to follow the latitudinal variation of the satellite. For density values above  $10^{-12}$  kg/m<sup>3</sup>, the CASSIOPE and the JB2008 ratios are close-fitting and centered to unit. In regards to the standard deviations of the density ratios (Figure 9, right panels), the CASSIOPE densities show a high performance with low deviations for density values above  $\sim 10^{-12}$  kg/m<sup>3</sup>. Then, the JB2008 (green) shows slightly lower deviations than the NRLMSISE-00 (red), in comparison to CASSIOPE; for density values of  $\sim 10^{-11}$  kg/m<sup>3</sup>, the CASSIOPE densities reach deviations of 2%, while the models only 10%. Then, for density

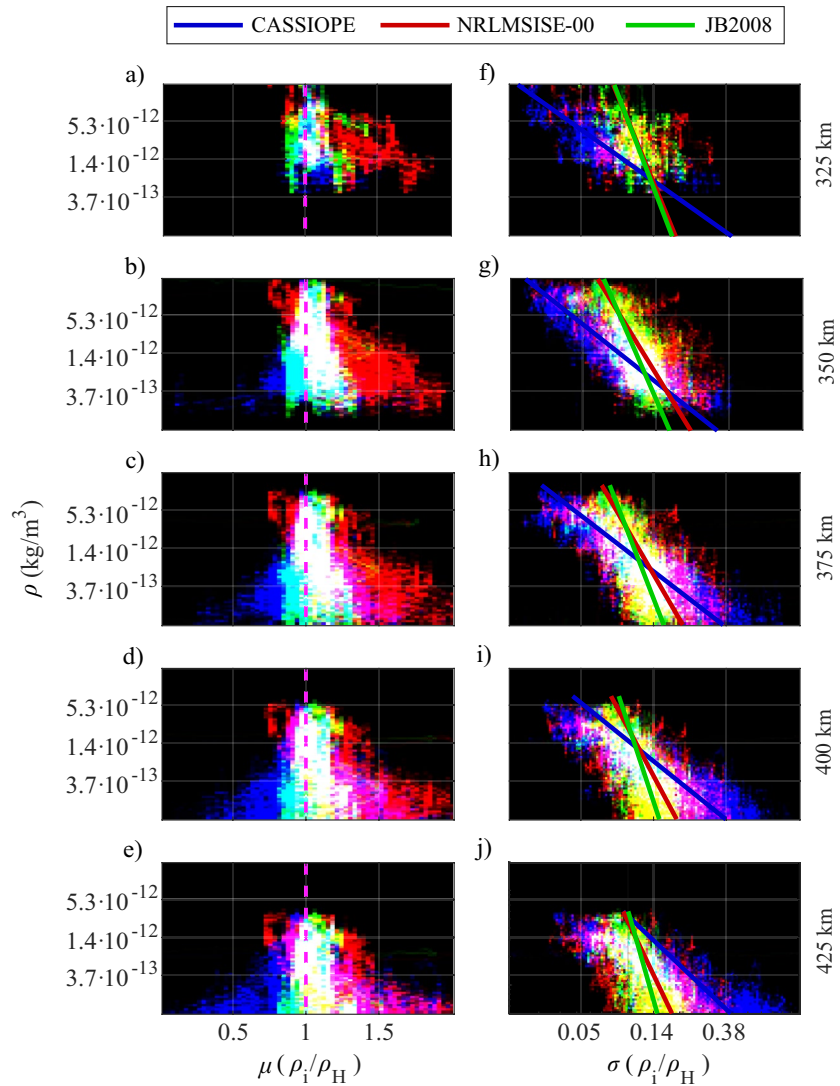


**Figure 9.** The composite Red-Green-Blue (RGB) scatter plots showing the background density (y-axes) versus the mean-averages of the ratios (on the left), and the corresponding standard deviations (on the right), for CAScade SmallSat and IOnospheric Polar Explorer (CASSIOPE), Naval Research Laboratory Mass Spectrometer and Incoherent Scatter Radar Exosphere/2000 (NRLMSISE-00), and Jacchia-Bowman/2008 (JB2008). Same values as Figures 4d and 4e to Figures 7d and 7e, for the altitudes of 325, 350, 375, 400, and 425 km, from top to bottom, respectively. The fits of the standard deviations are in the left panels. Note the logarithmic scale of the y-axis in the left panels. In the right panels, both axes are in logarithmic scale.

values below  $\sim 10^{-12}$  kg/m<sup>3</sup>, the CASSIOPE standard deviations increase in magnitude, reaching even 30% or more at  $\sim 10^{-13}$  kg/m<sup>3</sup>.

### 3.2. Density Disturbances Due to Magnetospheric Forcing

In Figure 10, the correlations and time delays between the  $E_m$  index and the density disturbances due to magnetospheric forcing, as seen by CASSIOPE, are shown for the altitudes of 350, 375, 400, and 425 km. In this figure, there is the inclusion of the identical analysis for the NRLMSISE-00 and the JB2008 densities, so that the performance of the time-response can be compared. We employ the filtered densities as described in Section 2, and perform the correlation-delay study at the different altitudes. In order to remove the “quiet” background density from the CASSIOPE densities, the JB2008 model is used due to its good performance. Here, we refer to “quiet” to the thermosphere estate in which the geomagnetic conditions are

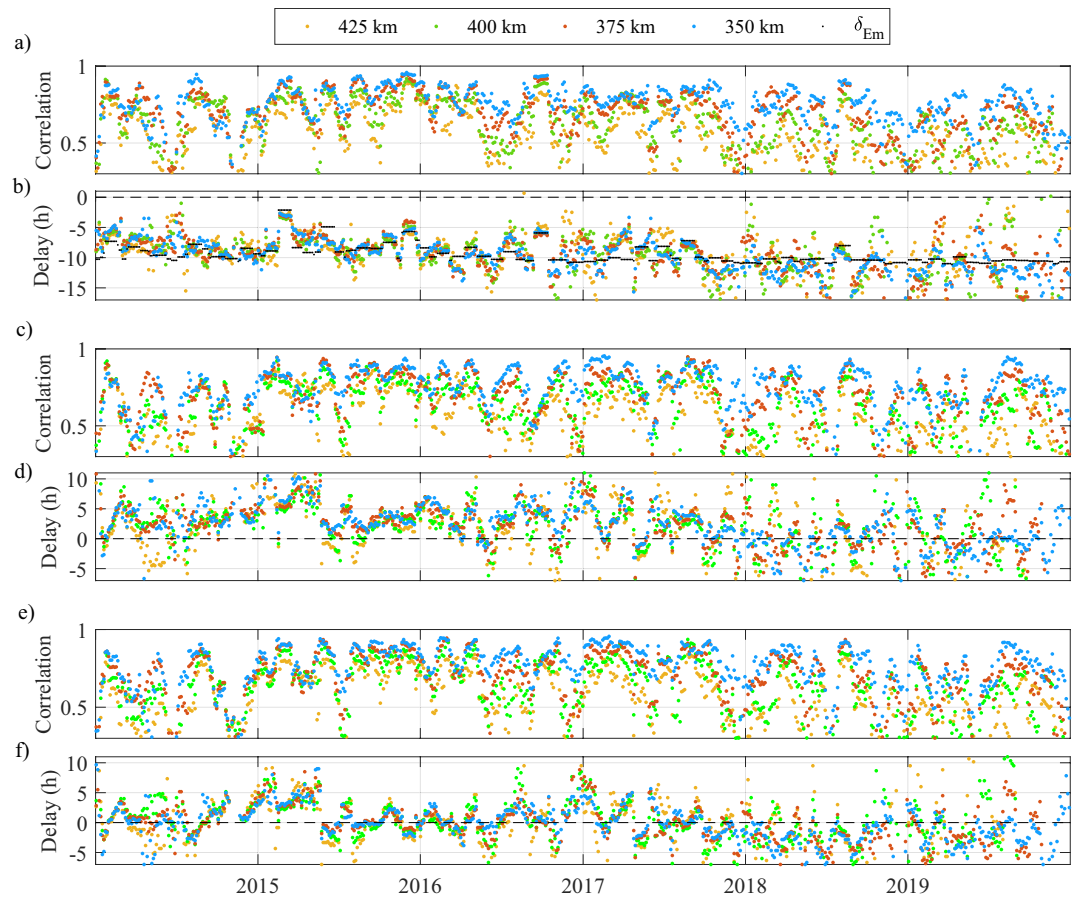


**Figure 10.** The 30-days running window of (a) correlation and (b) time delay between the  $E_m$  index and the density disturbances due to magnetospheric forcing at different altitudes. In (b) we also include the best fit in terms of the 30-days running window maximum  $E_m$  value. The identical analysis for the Naval Research Laboratory Mass Spectrometer and Incoherent Scatter Radar Exosphere/2000 (NRLMSISE-00) and the Jacchia-Bowman/2008 (JB2008) densities is shown in panels (c and d) and (e and f), respectively.

negligible. The “quiet” background was estimated by setting the inputs of magnetospheric forcing to zero in the models. For the NRLMSISE-00 and the JB2008 densities, their own “quiet” background is removed. Finally, the time delay estimated by the merging electric field  $E_m$  index is used to identify the activity periods, and to further compare and assess the time-delay responses from the models. Figure 11 shows the filtered densities from CASSIOPE and models for a case example using data from 2015.

In this analysis, an obvious dependence of the magnitude of the storm to the time delay response is found. For instance, in Figure 10b, the 30-days running window of the maximum value of  $E_m$  shows that the fit follows the fluctuations of the time delay. Table 3 shows the corresponding parameters to be used for the parameterization (Equation 2b), and Figure 11 shows the resulting fit for a case example on 2015. In Figure 10, no significant differences are seen in the time delay response at different altitudes. During quiet conditions, delay times are approximately 9–10 h, but these advance to 4–5 h following the intense storms. Clear examples are seen in March and December 2015, October 2016, September 2017, etc. During these storms, the correlations reach above 95% (Figure 10a). The mean correlation for the full time-series is approximately 75%. Lower correlations are seen during lower magnetospheric conditions (the magnitude of the time delay  $\delta_{E_m}$  to identify the storm periods).

Identical analyses were performed for the NRLMSISE-00 and the JB2008 densities, and these are shown in Figures 10c–10f. Here, the dependence of the magnitude of the storm to the time delay response is captured poorly by the models. For these, in the hypothetical case that the models provided a non-delayed response to the short-term variations, the time delays in Figures 10d and 10f should be zero. However, clear deviations

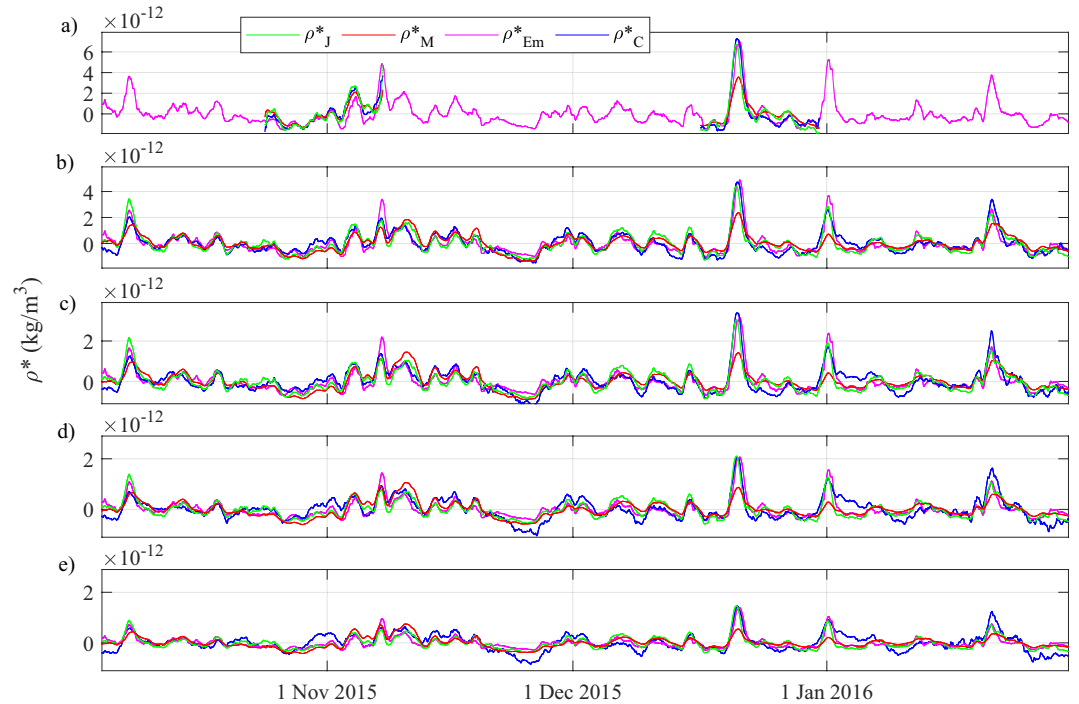


**Figure 11.** The density disturbances due to magnetospheric forcing at (a) 325 km, (b) 350 km, (c) 375 km, (d) 400 km, and (e) 425 km altitude, as seen by CAScade SmallSat and IONospheric Polar Explorer (CASSIOPE) ( $\rho_C^*$ ), Naval Research Laboratory Mass Spectrometer and Incoherent Scatter Radar Exosphere/2000 (NRLMSISE-00) ( $\rho_M^*$ ), acchia-Bowman/2008 (JB2008) ( $\rho_J^*$ ), and from the fit with  $E_m$  ( $\rho_{E_m}^*$ ). Case example during October 2015 to March 2016 with samples from inbound orbits. Data gaps in (a) are caused by the variable altitude of the satellites' perigee, which sometimes does not reach the altitude of 325 km. Note the different scales on the y-axes.

are seen with respect to the zero ( $\pm 5$  h), and a larger deviation during the low solar activity period (2018–2019). The most significant deviation can be seen during January–April 2015, where the NRLMSISE-00 densities show a retarded time-delay estimation of approximately 6.5 h, while the JB2008 4.5 h. More in detail, for the storm of March 2015, the NRLMSISE-00 densities show a lag in the time-delay estimation by approximately 5 h, while the JB2008 by only 2.5 h; for the storm of December 2015, the NRLMSISE-00 densities show 3 h later, while the JB2008 2 h earlier; for the storms of October 2016 and September 2017, the NRLMSISE-00 densities show a lag of 4 h, while the JB2008 0 h; etc. In general, during high solar flux conditions, the NRLMSISE-00 densities show to overestimate the time delay by approximately 4 h, while the JB2008 has, in average, an unbiased time delay response. During low solar flux conditions, the NRLMSISE-00 densities show in average an unbiased time delay response, while the JB2008 shows to anticipate the response by approximately 2.5 h.

**Table 3**  
Parameters for the Fit of Density Disturbances Due to Magnetospheric Forcing  $\rho_{E_m}^*$  (Equation 2) in Terms of Solar Flux  $F_{10.7}$  and  $E_m$  Indices

Altitude (km)	p1	p2	d1	d2
325	$1.474 \pm 0.008$	$-16 \pm 4$	$0.06 \pm 0.02$	$-12.3 \pm 0.8$
350	$1.033 \pm 0.003$	$-4 \pm 1$	$0.14 \pm 0.01$	$-12.3 \pm 0.3$
375	$0.664 \pm 0.002$	$-1 \pm 1$	$0.21 \pm 0.03$	$-12.4 \pm 0.4$
400	$0.436 \pm 0.002$	$-0.9 \pm 0.9$	$0.25 \pm 0.06$	$-11.4 \pm 0.6$
425	$0.291 \pm 0.001$	$-0.7 \pm 0.8$	$0.3 \pm 0.1$	$-10.8 \pm 0.6$

Note. Units of density in  $\text{kg/m}^3$ .

#### 4. Discussion

The validation of CASSIOPE GNSS-based thermospheric densities in this study proves that low-budget commercial-off-the-shelf dual-frequency GNSS receivers on board small satellites can be used for thermosphere monitoring at a higher resolution and accuracy than that of existing techniques (excluding accelerometers) and empirical models. For densities above  $10^{-12} \text{ kg/m}^3$ , the similarity of the CASSIOPE densities to the HASDM data set is significant, with unbiased trends, and smaller deviations than that provided by the models. However, for densities below  $10^{-12} \text{ kg/m}^3$ , some systematic deviations with respect to the HASDM densities are evident. As these are now recognized, it could be possible to

achieve even smaller systematic errors in the future. In order to address the future research directions, it is necessary to discuss the possible causes of the high-cadence variability (less than 6 min) shown by the CASSIOPE densities; either by looking for actual variations (winds, ionospheric drag, etc.) in the spacecraft's bumpy, vertical trajectory along the thermosphere, or by looking for instrumental or modeling errors.

As described in Section 3, the latitude dependence of the CASSIOPE densities relative to the HASDM is stronger for density values below  $10^{-12}$  kg/m<sup>3</sup>. One likely source of this variability could be systematic errors in the precise velocities and its variations after the smoothing filter. Another source of the discrepancies could be actual density or wind increases due to magnetospheric forcing at the aurora regions. These short-term features could not be well captured by the HASDM, resulting in the observed latitudinal systematic variation. In fact, this study shows the peaks of these fluctuations are certainly located at the latitudes of  $\sim 70^\circ$  in both hemispheres; a similar but less pronounced signature has been found in the NRLMSISE-00 and JB2008 models. Additional validations of these hypothesis could be performed by comparing accelerometer densities with the HASDM outputs in similar conditions. However, comparing accelerometer densities with the CASSIOPE densities is a difficult task since the existing accelerometer measurements are limited in quantity in both space (3 dimensions) and time.

The high resolution of the CASSIOPE densities is comparable to that of accelerometer density estimates (1 s interval), but the validation of high cadence density variability is still a challenge. The possible causes of the observed variability could be actual density variations, or caused by instrumental or modeling errors (e.g., ionospheric-delay models, winds model, etc.). As mentioned above, a possible test of these disturbances could be performed by comparing densities estimated by space accelerometers. However, adding more complexity to the previous considerations, we should take into account that existing missions carrying accelerometers have circular orbit configurations, and the highly variable altitude of the CASSIOPE satellite may cause additional sources or density variability, either from thermospheric winds (Bruinsma et al., 2004, 2006), ionospheric drag (Capon et al., 2019), or other factors. It is also important to consider vertical winds omitted in the estimation of densities, mostly due to the lack of existing empirical models to represent the vertical wind variability. Other validation schemes could include comparisons with ionospheric profiles from GNSS Radio Occultation (GNSS-RO) (Steiner et al., 2020) to reveal a possible ionospheric drag, or in-situ measurements of magnetic field, electric currents, etc (e.g., Heelis & Maute, 2020; Lu et al., 2020), which could correlate with the observed density variability, or even other sources of high-resolution measurements of temperature, density, composition, pressure, etc (e.g., Forbes et al., 2018; Tang et al., 2020).

## 5. Summary

In this paper, thermospheric mass densities inferred from interpolation and numerical differentiation of CASSIOPE GNSS-based precise orbits have been calculated, evaluated, and validated for the period 2014–2020. Here, it is proved the acceleration approach for high-resolution thermospheric mass density estimation can be used in current and/or future satellites with appropriate GNSS receivers, and without need of high-precision accelerometers. First, total accelerations are obtained by differentiating GNSS-based precise orbit velocities at a high-rate (e.g., 1 s interval), and the conservative and radiation pressure accelerations from conventional models can be subsequently subtracted. Finally, the density observation data are estimated from the resulting accelerations due to drag.

The HASDM density data set has been used as the control for the validation of the CASSIOPE densities, and we have compared the ratio of densities with that from the NRLMSISE-00 and JB2008 empirical models. Moreover, by setting the geomagnetic contributions to zero in the models, we isolated the density disturbances due to magnetospheric forcing from the CASSIOPE time-series, and investigated the correlations and time-delay responses to the models and to the merging electric field ( $E_m$ ) index. The results from our analyses are summarized as follows:

1. For density values above  $\sim 10^{-12}$  kg/m<sup>3</sup>, the CASSIOPE densities can provide better accuracy than the densities of the existing empirical models. The correlation of CASSIOPE with HASDM is  $\sim 5\%$  higher than that of the models, and the standard deviation is within 10% of the background density. It is significant that for density values of  $\sim 10^{-11}$  kg/m<sup>3</sup>, the CASSIOPE densities can reach deviations of 2%, where the models reach only 10%.

2. Comparisons with the NRLMSISE-00 and JB2008 models have shown the ratios of density, with respect to the HASDM data set, are highly variable in time, and increase with a low-density background. During low solar-flux conditions, NRLMSISE-00 largely overestimates both the CASSIOPE and the JB2008 densities by approximately 150%.
3. For density values below  $\sim 10^{-12}$  kg/m<sup>3</sup>, systematic errors have shown to reduce the precision of the CASSIOPE densities, and the models provide better performance. Although the new CASSIOPE GNSS-based densities were estimated at a second interval, the systematic errors originated in the POD scheme (stochastic least squares adjustment between models and GNSS observables) were observed in the form of noise and periodic errors to the final estimates. However, a systematic error has been found in the CASSIOPE densities, and therefore there is potential to achieve smaller deviations. The systematic variation shows to be a periodic fluctuation of 62.5-day period, which increases in amplitude with a low-density background. This period corresponds to the latitudinal variation of the satellite, and density increases/decreases are seen at higher/lower latitudes, respectively.
4. The time delay of density disturbances due to magnetospheric forcing have shown a linear dependence to the  $E_m$  index. Time delays to the  $E_m$  index have shown to be within the 4–7 h range during geomagnetic storms, while within 9–11 h during quiet conditions, and without significant dependence on altitude. This dependence is poorly captured by the models, showing clear deviated trends and localized discrepancies during severe storms. Both models show deviations in the range of  $\pm 5$  h. During low solar flux conditions, the NRLMSISE-00 shows in average an unbiased time delay response, while the JB2008 anticipates the response in approximately 2.5 h. During high solar flux conditions, the NRLMSISE-00 has an averaged overestimation of approximately 4 h, while the JB2008 shows an unbiased response.

With the increasing number of LEO satellites being equipped with a high-precision GNSS receivers and more enhanced data processing and orbit determination strategies, GNSS-based thermospheric mass densities can be used to investigate the geophysical processes in the upper atmosphere. In the near future, numerous datasets of GNSS-based densities will improve on the current limitation of lack of data, and the existing upper atmosphere models will be improved with unprecedented details. These models are very important for numerous applications, including the prediction of positioning disturbances due to aerodynamic drag acting on debris and artificial satellites, and space weather research. It is expected a new data set from other LEO missions will be provided.

## Appendix A: GNSS-Based Air-Drag Acceleration ( $a_D$ )

Instantaneous total accelerations ( $a_T$ ) are calculated through numerical differentiation of the GNSS-based precise orbit velocities. The 8-data point piece-wise Lagrange interpolation and a time-interval of 0.05 s is used for the numerical differentiation. At LEO altitudes, these settings allow the obtainment of an unbiased accuracy in the arc-to-chord threshold approach of approximately  $10^{-9}$  m/s<sup>2</sup> (Calabia et al., 2015). Subsequently, GNSS-based air-drag accelerations ( $a_D$ ) are retrieved by removing the gravitational ( $g$ ) and radiation pressure ( $a_R$ ) accelerations.

$$a_D = a_T - g - a_R \quad (\text{A1})$$

### A1. Gravitational Acceleration ( $g$ )

The gravitational accelerations ( $g$ ) are obtained from the combination of the static EGM2008 gravity field model with the background secular variations (Petit & Luzum, 2010). The Earth tides due to Sun and Moon (Wahr terms), the solid Earth pole tides (with sub-daily wobble variables), and the relativity corrections (Schwarzschild) are applied following the IERS2010 conventions (Petit & Luzum, 2010). The EOT11a ocean tides of Mayer-Gürr et al. (2012) is used, and the ocean pole tide of Desai (2002). Ephemeris of from Jet Propulsion Laboratory (JPL) DE421 are utilized to calculate the third body tides (Montenbruck & Gill, 2013). Then, the first derivative of the gravitational potential (Frommknecht, 2008) is used to compute the accelerations due to gravity.

## A2. Radiation Pressure Acceleration ( $a_R$ )

Radiation pressure accelerations include the direct solar radiation and the Earth's albedo ( $a_R = a_{sr} + a_{ea}$ ). The direct solar radiation ( $a_{sr}$ ) was formulated by Luthcke et al. (1997):

$$a_{sr} = \sum_{i=1}^{n_p} -\frac{E_{sr} A_i \hat{n}_i \cdot \hat{s}_{sun}^{sat}}{mc} \left[ 2 \left( \frac{c_{rd,i}}{3} + c_{rs,i} \hat{n}_i \cdot \hat{s}_{sun}^{sat} \right) \hat{n}_i + (1 - c_{rs,i}) \hat{s}_{sun}^{sat} \right] \quad (A2)$$

In this equation,  $n_p$  is the number of plates,  $A_i$  is the plate area,  $c$  is the speed of light,  $c_{rd,i}$  is the coefficient of diffusive reflectivity,  $c_{rs,i}$  is the coefficient of specular reflectivity,  $m$  is the satellite mass,  $\hat{n}_i$  is the unit plate normal,  $\hat{s}_{sun}^{sat}$  is the unit sun-satellite vector, and  $E_{sr} = sh \cdot 1366 \left( 1 \text{ AU} / s_{sun}^{sat} \right)^2$  is the flux on the Earth's atmosphere ( $1366 \text{ W/m}^2$ ), corrected from the yearly period of the Earth's orbit eccentricity and from the planetary eclipse ratio ( $sh$ ) (Montenbruck & Gill, 2013).

Similarly, the Earth albedo acceleration ( $a_{ea}$ ) can be computed as follows:

$$a_{ea} = \sum_{i=1}^{n_p} \sum_{j=1}^{grid} -\frac{E_{ea,j} A_j \hat{n}_i \cdot \hat{s}_j^{sat}}{mc} \left[ 2 \left( \frac{c_{rd,i}}{3} + c_{rs,i} \hat{n}_i \cdot \hat{s}_j^{sat} \right) \hat{n}_i + (1 - c_{rs,i}) \hat{s}_j^{sat} \right] \quad (A3)$$

In this equation, the parameter  $E_{ea,j} = E_{ea}^R + E_{ea}^{IR}$  is the combination of the radiation reflected at the Earth's surface  $E_{ea}^R$  and the Earth's infrared radiation  $E_{ea}^{IR}$ . The Earth's reflected solar radiation  $E_{ea}^R$  at each satellite position is estimated using the monthly averages of the NASA's Total Ozone Mapping Spectrometer (TOMS) reflectivity index ( $\sigma$ ) (Bhanderi, 2005):

$$E_{ea,j}^R = f_j v_j E_{sr} \frac{A_j (\hat{n}_j \cdot \hat{s}_j^{sun}) (\hat{n}_j \cdot \hat{s}_j^{sat}) \sigma_j}{\pi |\hat{s}_j^{sat}|^2} \quad (A4)$$

In this equation,  $f_j$  is field of view of the satellite,  $v_j$  is the sunlight function, and  $A_j$  is the area of each cell  $j$  of TOMS. The reflection angle on each cell is defined by the directions of the satellite  $\hat{s}_j^{sat}$ , the Sun  $\hat{s}_j^{sun}$ , and the cell normal-vector  $\hat{n}_j$ .

The Earth's infrared radiation  $E_{ea}^{IR}$  can be modeled as a black body with a surface temperature of 288 K, whose spectrum is mainly IR with an exitance of about  $239 \text{ W/m}^2$  (Taylor, 2005). In a similar way, the IR irradiance  $E_{ea,j}^{IR}$  from each visible cell  $j$  of the Earth's surface has been computed as follows:

$$E_{ea,j}^{IR} = f_j 239 \left( \frac{1 \text{ AU}}{s_{sun}^j} \right)^2 e_{IR,j} \frac{A_j \hat{n}_j \cdot \hat{s}_j^{sat}}{\pi |\hat{s}_j^{sat}|^2} \quad (A5)$$

In this equation, the Earth IR radiation  $e_{IR,j}$  for each cell  $j$  was parameterized in terms of latitude and season by Knocke and Ries (1987):

$$e_{IR} = e_0 + e_1 P_1 \sin \varphi + e_2 P_2 \sin \varphi \quad (A6)$$

$$e_1 = k_0 + k_1 \cos [\omega (JD - t_0)] + k_2 \sin [\omega (JD - t_0)] \quad (A7)$$

Here,  $t_0$  is the epoch of December 22, 1981,  $\omega$  is the Earth orbit rotation rate around the Sun ( $2\pi/365.5$ ),  $\varphi$  is the equatorial geocentric latitude,  $JD$  is the Julian Date,  $P_n$  is the Legendre polynomial of degree  $n$ , and  $e_0 = 0.68$ ;  $e_2 = -0.18$ ;  $k_0 = 0$ ;  $k_1 = -0.07$ , and  $k_2 = 0$ .

Detailed algorithms and accurate schemes to estimate irradiative accelerations can be found in numerous works, for example, Calabia and Jin (2017), Doornbos (2011), Jin et al. (2018), Sutton (2008), Vielberg and Kusche (2020), Wöske et al. (2019), and the approximated values of CASSIOPE's panel properties are given in Calabia and Jin (2021a), where the visible (VIS) and the infrared (IR) part of the electromagnetic spectrum can be weighted by the amount of solar flux given for each spectral window (43% for VIS, and 53% for IR).

## Appendix B: Thermospheric Mass Density ( $\rho$ ) Retrieval

GNSS-based thermospheric mass densities are computed using the drag-force ( $F_D$ ) formula:

$$F_D = a_D m = \frac{1}{2} C_D A \rho v_r^2 \quad (\text{B1})$$

In this equation,  $a_D$  is the acceleration due to air-drag,  $m$  is the mass of the satellite,  $C_D$  is the drag coefficient,  $\rho$  is the thermospheric mass density, and  $A$  is the cross-sectional area perpendicular to the relative velocity of the atmosphere with respect to the spacecraft  $v_r$ , which includes the co-rotating atmosphere and the horizontal winds. Horizontal wind velocities are calculated from the horizontal wind model HWM14 (Drob et al., 2015), and the velocity of the co-rotating atmosphere is computed as the vector product between the Earth's angular rotation and the satellite's position vector. In this study, a variable drag coefficient  $C_D$  is approximated for the CASSIOPE satellite in terms of solar flux and altitude. Modification of the values is provided by Pardini et al. (2006) and for the hexagonal-prism shape of the CASSIOPE satellite using the results of Walker et al. (2014).

## Conflict of Interest

The authors declare no conflicts of interest relevant to this study.

## Data Availability Statement

The CASSIOPE precise orbit data are publicly available from <https://epop-data.phys.ucalgary.ca> and <https://swarm-diss.eo.esa.int>. The reflectivity data are available from the Total Ozone Mapping Spectrometer (TOMS) project, <http://disc.sci.gsfc.nasa.gov/acdisc/TOMS>. The HASDM density data are provided for scientific use courtesy of SET. The space weather data are available from the website of the Low Resolution OMNI (LRO) data set of NASA, <http://omniweb.gsfc.nasa.gov/form/dx1.html>. The merging electric field  $E_m$  is computed with the NASA's space weather data following the indications of Liu et al. (2010). The geomagnetic data are available from the International Service of Geomagnetic Indices (ISGI), [http://isgi.unistra.fr/data\\_download.php](http://isgi.unistra.fr/data_download.php). Density data supporting the findings of this study (Calabia & Jin, 2021b) are available at <http://doi.org/10.5281/zenodo.5079186>.

## Acknowledgments

This work was supported by the National Natural Science Foundation of China (NSFC) Project (Grant No. 12073012), the Startup Foundation for Introducing Talent of NUIST (Grant No. 2243141801036), and the Talent Start-Up Funding project of NUIST (Grant No. 1411041901010). Great appreciation is extended to CASSIOPE/e-POP team at the University of Calgary for providing the precise orbit data, to NASA and ISGI for the space weather and geomagnetic indices, to Dr. Kent Tobiska at SET for the HASDM density data, and to the NRLMSISE-00 and JB2008 teams for making the models publicly available. The authors are very thankful to the anonymous reviewers, Dr. Jiandong Liu, and Ms. Catherine M Jones for their revisions and suggestions to improve a previous version of the manuscript.

## References

- Anderson, R. L., George, H. B., & Forbes, J. M. (2009). Sensitivity of orbit predictions to density variability. *Journal of Spacecraft and Rockets*, 46(6), 1214–1230. <https://doi.org/10.2514/1.42138>
- Bates, D. R. (1959). Some problems concerning the terrestrial atmosphere above 100 km level. *Proceedings of the Royal Society A*, 253, 451–462. <https://doi.org/10.1098/rspa.1959.0207>
- Bhandari, D. (2005). *Spacecraft attitude determination with Earth albedo corrected sun sensor measurements*. Aalborg University.
- Blossfeld, M., Schmidt, M. K. B., Forootan, E., Calabia, A., Prol, F., & Soja, B. (2019). GGOS focus area on geodetic space weather research — Observation techniques and modeling approaches. *AGU Fall Meeting Abstracts*.
- Bowman, B. R., Marcos, F. A., & Kendra, M. J. (2004). *A method for computing accurate daily atmospheric density values from satellite drag data* (pp. 17). AAS/AIAA Spaceflight Mechanics Meeting.
- Bowman, B. R., & Storz, M. F. (2003). *High accuracy satellite drag model (HASDM) review*. AAS/AIAA Astrodynamics Specialist Conference.
- Bowman, B. R., Tobiska, W. K., Marcos, F. A., Huang, C. Y., Lin, C. S., and Burke, W. J. (2008). *A new empirical thermospheric density model JB2008 using new solar and geomagnetic indices*. AIAA/AAS Astrodynamics Specialist Conference.
- Bruinsma, S., & Biancale, R. (2003). Total densities derived from accelerometer data. *Journal of Spacecraft and Rockets*, 40(2), 230–236. <https://doi.org/10.2514/2.3937>
- Bruinsma, S., Forbes, J. M., Nerem, R. S., & Zhang, X. (2006). Thermosphere density response to the 20–21 November 2003 solar and geomagnetic storm from CHAMP and GRACE accelerometer data. *Journal of Geophysical Research*, 111, A06303. <https://doi.org/10.1029/2005ja011284>
- Bruinsma, S., Tamagnan, D., & Biancale, R. (2004). Atmospheric densities from CHAMP/STAR accelerometer observations. *Planetary and Space Science*, 52, 297–312. <https://doi.org/10.1016/j.pss.2003.11.004>
- Calabia, A., & Jin, S. G. (2016). New modes and mechanisms of thermospheric mass density variations from GRACE accelerometers. *Geophysical Research: Space Physics*, 121, 191–11. <https://doi.org/10.1002/2016JA022594>
- Calabia, A., & Jin, S. G. (2016). *Thermospheric mass density variations during the March 2015 geomagnetic storm from GRACE accelerometers* (pp. 4976–4980). Proceeding of Progress In Electromagnetics Research Symposium (PIERS2016). <https://doi.org/10.1109/PIERS.2016.7735812>
- Calabia, A., & Jin, S. G. (2017). Thermospheric density estimation and responses to the March 2013 geomagnetic storm from GRACE GPS-determined precise orbits. *Journal of Atmospheric and Solar-Terrestrial Physics*, 154, 167–179. <https://doi.org/10.1016/j.jastp.2016.12.011>

- Calabia, A., & Jin, S. G. (2019). Solar-cycle, seasonal, and asymmetric dependencies of thermospheric mass density disturbances due to magnetospheric forcing. *Annales Geophysicae*, 37, 989–1003. <https://doi.org/10.5194/angeo-37-989-2019>
- Calabia, A., & Jin, S. G. (2020). New modes and mechanisms of long-term ionospheric TEC variations from Global Ionosphere Maps. *Journal of Geophysical Research - A: Space Physics*, 125(6), e2019JA027703. <https://doi.org/10.1029/2019JA027703>
- Calabia, A., & Jin, S. G. (2021a). Upper-atmosphere mass density variations from CASSIOPE precise orbits. *Space Weather*, 19, e2020SW002645. <https://doi.org/10.1029/2020SW002645>
- Calabia, A., & Jin, S. G. (2021b). CASSIOPE GNSS-based thermospheric mass densities from 325 to 425 km at intervals of 25 km (Data set). Zenodo. <https://doi.org/10.5281/zenodo.5079186>
- Calabia, A., Jin, S. G., & Tenzer, R. (2015). A new GPS-based calibration of GRACE accelerometers using the arc-to-chord threshold uncovered sinusoidal disturbing signal. *Aerospace Science and Technology*, 45, 265–271. <https://doi.org/10.1016/j.ast.2015.05.013>
- Calabia, A., Tang, G., & Jin, S. G. (2020). Assessment of new thermospheric mass density model using NRLMSISE-00 model, GRACE, Swarm-C, and APOD observations. *Journal of Atmospheric and Solar-Terrestrial Physics*, 199, 105207. <https://doi.org/10.1016/j.jastp.2020.105207>
- Capon, C. J., Smith, B., Brown, M., Abay, R., & Boyce, R. R. (2019). Effect of ionospheric drag on atmospheric density estimation and orbit prediction. *Advances in Space Research*, 63(8), 2495–2505. <https://doi.org/10.1016/j.asr.2019.01.013>
- Chen, G. M., Xu, J., Wang, W., & Burns, A. G. (2014). A comparison of the effects of CIR- and CME-induced geomagnetic activity on thermospheric densities and spacecraft orbits: Statistical studies. *Geophysical Research: Space Physics*, 119, 7928–7939. <https://doi.org/10.1002/2014JA019831>
- Desai, S. D. (2002). Observing the pole tide with satellite altimetry. *Journal of Geophysical Research*, 107(C11), 3186. <https://doi.org/10.1029/2001JC001224>
- Doornbos, E. (2011). *Thermospheric density and wind determination from satellite dynamics*. TU Delft.
- Doornbos, E., J van den IJssel, H. L., Foerster, M., Koppenwallner, G., Bruinsma, S., Sutton, E., et al. (2010). Neutral density and crosswind determination from arbitrarily oriented triaxial accelerometers on satellites. *Journal of Spacecraft and Rockets*, 47, 580–589. <https://doi.org/10.2514/1.48114>
- Drob, D. P., Emmert, J. T., Meriwether, J. W., Makela, J. J., Doornbos, E., Conde, M., et al. (2015). An update to the Horizontal Wind Model (HWM): The quiet time thermosphere. *Earth and Space Science*, 2, 301–319. <https://doi.org/10.1002/2014EA000089>
- Echer, E., Gonzalez, W. D., Gonzalez, A. L. C., Prestes, A., Vieira, L. E. A., dal Lago, A., et al. (2004). Long-term correlation between solar and geomagnetic activity. *Journal of Atmospheric and Solar-Terrestrial Physics*, 66, 1019–1025. <https://doi.org/10.1016/j.jastp.2004.03.011>
- Emmert, J. T., & Picone, J. M. (2010). Climatology of globally averaged thermospheric mass density. *Journal of Geophysical Research*, 115, A09326. <https://doi.org/10.1029/2010JA015298>
- Forbes, J., Zhang, X., Maute, A., & Hagan, M. E. (2018). Zonally symmetric oscillations of the thermosphere at planetary wave periods. *Journal of Geophysical Research - A: Space Physics*, 123, 41104128. <https://doi.org/10.1002/2018JA025258>
- Frommknecht, B. (2008). *Integrated sensor analysis of the GRACE mission*. Verlag der Bayerischen Akademie der Wissenschaften.
- Heelis, R. A., & Maute, A. (2020). Challenges to understanding the Earth's ionosphere and thermosphere. *Geophysical Research: Space Physics*, 125, e2019JA027497. <https://doi.org/10.1029/2019ja027497>
- Horvath, I., & Lovell, B. C. (2018). High-latitude neutral density structures investigated by utilizing multi-instrument satellite data and NRLMSISE-00 simulations. *Geophysical Research: Space Physics*, 123, 1663–1677. <https://doi.org/10.1002/2017JA024600>
- Jackson, D. R., Bruinsma, S., Negrin, S., Stolle, C., Budd, C. J., Dominguez Gonzalez, R., et al. (2020). The space weather atmosphere models and indices (SWAMI) project: Overview and first results. *Journal of Space Weather and Space Climate*, 10, 18. <https://doi.org/10.1051/swsc/20200019>
- Jin, S., Han, L., & Cho, J. (2011). Lower atmospheric anomalies following the 2008 Wenchuan Earthquake observed by GPS measurements. *Journal of Atmospheric and Solar-Terrestrial Physics*, 73(7-8), 810–814. <https://doi.org/10.1016/j.jastp.2011.01.023>
- Jin, S., Jin, R., & Kutoglu, H. (2017). Positive and negative ionospheric responses to the March 2015 geomagnetic storm from BDS observations. *Journal of Geodesy*, 91(6), 613–626. <https://doi.org/10.1007/s00190-016-0988-4>
- Jin, S. G., Calabia, A., & Yuan, L. L. (2018). Thermospheric sensing from GNSS and accelerometer on small satellites (Vol. 99, pp. 1–495). Proceedings of the IEEE. <https://doi.org/10.1109/JPROC.2018.2796084>
- Jin, S. G., & Su, K. (2020). PPP models and performances from single- to quad-frequency BDS observations. *Satellite Navigation*, 1(1), 16. <https://doi.org/10.1186/s43020-020-00014-y>
- Kan, J. K., & Lee, L. C. (1979). Energy coupling function and solar wind-magnetosphere dynamo. *Geophysical Research Letters*, 6(7), 577–580. <https://doi.org/10.1029/gl006i007p00577>
- Kim, D., & Langley, R. B. (2019). The GPS attitude, positioning, and profiling experiment for the enhanced polar outflow probe platform on the Canadian CASSIOPE satellite. *Geomatica*, 64(2), 233–243. <https://doi.org/10.5623/geomat-2010-0023>
- Knocke, P., & Ries, J. (1987). Earth radiation pressure effects on satellites. In *Center for space research technical memorandum, CSR-TM-87-01*. The University of Texas at Austin.
- Li, R., & Lei, J. (2020). Responses of thermospheric mass densities to the October 2016 and September 2017 geomagnetic storms revealed from multiple satellites observations. *Geophysical Research: Space Physics*, 125, e2020JA028534. <https://doi.org/10.1029/2020JA028534>
- Liu, H., & Lühr, H. (2005). Strong disturbance of the upper thermospheric density due to magnetic storms: CHAMP observations. *Journal of Geophysical Research*, 110, A09S29. <https://doi.org/10.1029/2004JA010908>
- Liu, R., Lühr, H., Doornbos, E., & Ma, S. Y. (2010). Thermospheric mass density variations during geomagnetic storms and a prediction model based on the merging electric field. *Annales Geophysicae*, 28, 1633–1645. <https://doi.org/10.5194/angeo-28-1633-2010>
- Lu, G., Zakharenkova, I., Cherniak, I., & Dang, T. (2020). Large-scale ionospheric disturbances during the 17 March 2015 storm: A model-data comparative study. *Journal of Geophysical Research - A: Space Physics*, 125, e2019JA027726. <https://doi.org/10.1029/2019JA027726>
- Lühr, H., Rother, M., Köhler, W., Ritter, P., & Grunwaldt, L. (2004). Thermospheric up-welling in the cusp region: Evidence from CHAMP observations. *Geophysical Research Letters*, 31, L06805. <https://doi.org/10.1029/2003GL019314>
- Luthcke, S. B., Marshall, J. A., Rowton, S. C., Rachlin, K. E., Cox, C. M., & Williamson, R. G. (1997). Enhanced radiative force modeling of the tracking and data relay satellites. *Journal of the Astronautical Sciences*, 45(3), 349–370. <https://doi.org/10.1007/bf03546409>
- March, G., Doornbos, E., & Visser, P. (2019). High-fidelity geometry models for improving the consistency of CHAMP, GRACE, GOCE, and Swarm thermospheric density data sets. *Advances in Space Research*, 63(1), 213–238. <https://doi.org/10.1016/j.asr.2018.07.009>
- March, G., Visser, T., Visser, P. N. A. M., & Doornbos, E. N. (2019). CHAMP and GOCE thermospheric wind characterization with improved gas-surface interactions modelling. *Advances in Space Research*, 64(6), 1225–1242. <https://doi.org/10.1016/j.asr.2019.06.023>
- Marcos, F. A., & Forbes, J. M. (1985). Thermospheric winds from the satellite electrostatic triaxial accelerometer system. *Journal of Geophysical Research*, 90, 6543–6552. <https://doi.org/10.1029/JA090iA07p06543>

- Mayer-Gürr, T. R. S., Bosch, W., Daras, I., Flechtner, F., Dahle, C., & Dahle, C. (2012). Ocean tides from satellite altimetry and GRACE. *Journal of Geodynamics*, 59–60, 28–38. <https://doi.org/10.1016/j.jog.2011.10.009>
- Mehta, P. M., Walker, A., McLaughlin, C. A., & Koller, J. (2014). Comparing physical drag coefficients computed using different gas–surface interaction models. *Journal of Spacecraft and Rockets*, 51(3), 873–883. <https://doi.org/10.2514/1.A32566>
- Mehta, P. M., Walker, A. C., Sutton, E. K., & Godinez, H. C. (2017). New density estimates derived using accelerometers on board the CHAMP and GRACE satellites. *Space Weather*, 15, 558–576. <https://doi.org/10.1002/2016SW001562>
- Montenbruck, O., & Gill, E. (2013). *Satellite orbits: Models, methods and applications*. Berlin: Springer.
- Montenbruck, O., Hauschild, A., Langley, R. B., & Siemes, C. (2019). CASSIOPE orbit and attitude determination using commercial off-the-shelf GPS receivers. *GPS Solutions*, 23, 114. <https://doi.org/10.1007/s10291-019-0907-2>
- Okoh, D., Onwuneme, S., Seemala, G., Jin, S., Rabiou, B., Nava B., & Uwamahoro, J. (2018). Assessment of the NeQuick-2 and IRI-Plas 2017 models using global and long-term GNSS measurements. *Journal of Atmospheric and Solar-Terrestrial Physics*, 170, 1–10. <https://doi.org/10.1016/j.jastp.2018.02.006>
- Oliveira, D. M., & Zesta, E. (2019). Satellite orbital drag during magnetic storms. *Space Weather*, 17, 1510–1533. <https://doi.org/10.1029/2019SW002287>
- Palmroth, M., Grandin, M., Sarris, T., Doornbos, E., Tourgaidis, S., Aikio, A., et al. (2021). Lower-thermosphere-ionosphere (LTI) quantities: Current status of measuring techniques and models. *Annales Geophysicae*, 39, 189–237. <https://doi.org/10.5194/angeo-39-189-2021>
- Pardini, C., Tobiska, W. K., & Anselmo, L. (2006). Analysis of the orbital decay of spherical satellites using different solar flux proxies and atmospheric density models. *Advances in Space Research*, 37(2), 392–400. <https://doi.org/10.1016/j.asr.2004.10.009>
- Petit, G., & Luzum, B. (2010). *IERS conventions (2010), IERS technical note 36, international Earth rotation and reference systems Service (IERS)*. Verlag des Bundesamts für Kartographie und Geodäsie.
- Picone, J. M., Hedin, A. E., Drob, D. P., & Aikin, A. C. (2002). NRLMSISE-00 empirical model of the atmosphere: Statistical comparisons and scientific issues. *Journal of Geophysical Research*, 107(A12), 1468. <https://doi.org/10.1029/2002JA009430>
- Pilinski, M. D., Argrow, B. M., & Palo, S. E. (2011). Drag coefficients of satellites with concave geometries: Comparing models and observations. *Journal of Spacecraft and Rockets*, 48(2), 312–325. <https://doi.org/10.2514/1.50915>
- Qian, L., & Solomon, S. C. (2012). Thermospheric density: An overview of temporal and spatial variations. *Space Science Reviews*, 168, 147–173. <https://doi.org/10.1007/s11214-011-9810-z>
- Siemes, C. J., de Teixeira da Encarnação, J., Doornbos, E., van den IJssel, J., Kraus, J., Grunwaldt, L., et al. (2016). Swarm accelerometer data processing from raw accelerations to thermospheric neutral densities. *Earth Planets and Space*, 68(1), 92. <https://doi.org/10.1186/s40623-016-0474-5>
- Steiner, A. K., Ladstädter, F., Ao, C. O., Gleisner, H., Ho, S. P., Hunt, D., et al. (2020). Consistency and structural uncertainty of multi-mission GPS radio occultation records. *Atmospheric Measurement Techniques*, 13, 2547–2575. <https://doi.org/10.5194/amt-13-2547-2020>
- Storz, M. F., Bowman, B. R., Branson, M. J. I., Casali, S. J., & Tobiska, W. K. (2005). High accuracy satellite drag model (HASDM). *Advances in Space Research*, 36(12), 2497–2505. <https://doi.org/10.1016/j.asr.2004.02.020>
- Sutton, E. K. (2008). *Effects of solar disturbances on the thermosphere densities and winds from CHAMP and GRACE satellite accelerometer data*. University of Colorado.
- Sutton, E. K., Forbes, J. M., & Nerem, R. S. (2005). Global thermospheric neutral density and wind response to the severe 2003 geomagnetic storms from CHAMP accelerometer data. *Journal of Geophysical Research*, 110, A09S40. <https://doi.org/10.1029/2004ja010985>
- Tang, G. S., Li, X., Cao, J. S. L., Chen, G., Haijun, M., Zhang, X., et al. (2020). APOD mission status and preliminary results. *Science China Earth Sciences*, 63, 257–266. <https://doi.org/10.1007/s11430-018-9362-6>
- Taylor, F. W. (2005). *Elementary climate physics*. U Press.
- Tobiska, W. K., Bowman, B. R., Bouwer, D., Cruz, A., Wahl, K., Pilinski, M., et al. (2021). The SET HASDM density database. *Space Weather*, 19, e2020SW002682. <https://doi.org/10.1029/2020SW002682>
- van den IJssel, J., Doornbos, E., Iorfida, E., March, G., Montenbruck, O., & Montenbruck, O. (2020). Thermosphere densities derived from Swarm GPS observations. *Advances in Space Research*, 65(7), 1758–1771. <https://doi.org/10.1016/j.asr.2020.01.004>
- Vielberg, K., & Kusche, J. (2020). Extended forward and inverse modeling of radiation pressure accelerations for LEO satellites. *Journal of Geodesy*, 94, 43. <https://doi.org/10.1007/s00190-020-01368-6>
- Walker, A., Mehta, P., & Koller, J. (2014). Drag coefficient model using the cercignani-lampis-lord gas-surface interaction model. *Journal of Spacecraft and Rockets*, 51(5), 1544–1563. <https://doi.org/10.2514/1.A32677>
- Wöske, F., Kato, T., Rievers, B., & List, M. (2019). GRACE accelerometer calibration by high precision non-gravitational force modeling. *Advances in Space Research*, 63(3), 1318–1335. <https://doi.org/10.1016/j.asr.2018.10.025>
- Yau, A. W., James, H. G., & Liu, W. (2006). The Canadian enhanced polar outflow probe (e-POP) mission in ILWS. *Advances in Space Research*, 38(8), 1870–1877. <https://doi.org/10.1016/j.asr.2005.01.058>
- Yuan, L., Jin, S., & Calabia, A. (2019). Distinct thermospheric mass density variations following the September 2017 geomagnetic storm from GRACE and Swarm. *Journal of Atmospheric and Solar-Terrestrial Physics*, 184, 30–36. <https://doi.org/10.1016/j.jastp.2019.01.007>